Available online at www.sciencedirect.com
ScienceDirect
Journal of Computational Physics 226 (2007) 1271–1290
JOURNAL OF COMPUTATIONAL PHYSICS
www.elsevier.com/locate/jcp

Diffusion on a curved surface coupled to diffusion in the volume: Application to cell biology

Igor L. Novak [a,*], Fei Gao [a], Yung-Sze Choi [b], Diana Resasco [c], James C. Schaff [a], Boris M. Slepchenko [a,*]

[a] *Center for Cell Analysis and Modeling, Department of Cell Biology, University of Connecticut Health Center, Farmington, CT 06030, United States*
[b] *Department of Mathematics, University of Connecticut, Storrs, CT 06269, United States*
[c] *Department of Computer Science, Yale University, New Haven, CT 06520, United States*

Received 18 May 2006; received in revised form 18 May 2007; accepted 22 May 2007
Available online 8 June 2007

Abstract

An algorithm is presented for solving a diffusion equation on a curved surface coupled to diffusion in the volume, a problem often arising in cell biology. It applies to pixilated surfaces obtained from experimental images and performs at low computational cost. In the method, the Laplace–Beltrami operator is approximated locally by the Laplacian on the tangential plane and then a finite volume discretization scheme based on a Voronoi decomposition is applied. Convergence studies show that mass conservation built in the discretization scheme and cancellation of sampling error ensure convergence of the solution in space with an order between 1 and 2. The method is applied to a cell-biological problem where a signaling molecule, G-protein Rac, cycles between the cytoplasm and cell membrane thus coupling its diffusion in the membrane to that in the cell interior. Simulations on realistic cell geometry are performed to validate, and determine the accuracy of, a recently proposed simplified quantitative analysis of fluorescence loss in photobleaching. The method is implemented within the Virtual Cell computational framework freely accessible at www.vcell.org.

Keywords: Diffusion on a curved surface; Laplace–Beltrami operator; Voronoi decomposition; Finite volume discretization; Sampling noise; Fluorescence loss in photobleaching; Dissociation rate constant

1. Introduction

Recently, there has been increased attention to numerical approaches to diffusion on arbitrary surfaces, particularly in the context of applications to cell biology [1,2]. Indeed, cellular metabolism and signaling are mediated in part by trans-membrane receptors that can diffuse in the cell membrane [3]. Because the cell

* Corresponding authors. Tel.: +1 860 679 3997/4025; fax: +1 860 679 1039.
E-mail addresses: novak@uchc.edu (I.L. Novak), fgao@uchc.edu (F. Gao), choi@math.uconn.edu (Y.-S. Choi), resasco@cs.yale.edu (D. Resasco), schaff@neuron.uchc.edu (J.C. Schaff), boris@neuron.uchc.edu (B.M. Slepchenko).

0021-9991/$ - see front matter © 2007 Elsevier Inc. All rights reserved.
doi:10.1016/j.jcp.2007.05.025

shape is generally irregular, modeling these processes as well as the analysis of experimental data (see the application in part II) requires an accurate approximation of diffusion on an arbitrary curved surface. As in the flat space, a reaction–diffusion system on a surface $S \subset R^3$ is governed by mass conservation:

$$\frac{\partial C_i}{\partial t} = -\mathrm{div}_S \mathbf{J}_i + R_i, \quad i = 1, \ldots, m, \tag{1}$$

where C_i is the concentration of the ith membrane species, $\mathbf{J}_i = -D_i \,\mathrm{grad}_S\, C_i$ is the diffusive flux density of this species, D_i is the diffusion coefficient and the source term R_i describes the effect of all reactions on the ith species. The differential operators div_S and grad_S are defined on S and the second-order differential operator $\mathrm{div}_S\,(\mathrm{grad}_S) \equiv \Delta_S$ that appears in Eq. (1) is the Laplace–Beltrami operator (LBO) [4], which is a generalization of the Laplacian on manifolds.[1]

Spatial discretization of LBO for solving Eq. (1) numerically is generally more involved than in the flat case. While algorithms based on LBO discretization on triangulated surfaces [5] are relatively simple and fast, they involve unstructured grids and therefore may have a lower order of accuracy (see references in [5]). Better accuracy can be achieved by methods that embed the original two-dimensional (2D) problem into a three-dimensional (3D) space [1,2,6]. In [1], 2D diffusion on a surface is approximated by diffusion in an annular 3D domain consisting of all the points within a small, on the order of the mesh spacing h, distance from S, and the problem is solved on a uniform Cartesian grid. The papers [2,6] use another approach, originally introduced in [7]. In this approach, the initial data on the surface is extended smoothly into the 3D volume using a level set method (so that the surface S is a zero level set) and the equations are modified to exclude diffusive fluxes between the level sets. The adapted equations are solved in [6] on a uniform Cartesian grid, while spatial discretization in [2] is based on a particle representation of the implicit surfaces (the particle methods were previously used in [8] for solving diffusion in the lumen of the endoplasmic reticulum). Both methods [1,2] achieve second-order convergence in space and time. An additional advantage of the methods based on level sets is that they can be extended to accurate discretization of non-linear differential operators on surfaces. They also are suited well for problems involving moving membranes. Recently, the ideas of [7] have been further developed in [9] and applied in the context of phase field approximation in [10].

In biological applications, surfaces might not be given but rather need to be inferred from image data. The algorithms of [1,2] were used in conjunction with standard (albeit elaborate) methods for generating level set functions from image data for the purpose of constructing discretizations. The problem of recovering a smooth surface from pixilated data is currently an area of active research in the context of computer graphics [11]. A number of interesting approaches have been proposed. They usually involve an iterative process requiring significant user input, and therefore may not be easily automated. In addition, as these techniques are designed primarily for visualization purposes, they may be hard to apply in a way that guarantees convergence of surface metrics as the grid is refined.

Conservation of mass is important for computational modeling in cell biology. While the method of [6] is non-conservative, in [2] mass conservation is enforced through global rescaling, and the discretization scheme in [1] is fully conservative. Problems in which diffusion on the surface is coupled to diffusion in the enclosed volume often arise in cell biology. While [2] contains simulations of diffusion in the lumen and on the surface of the same geometry, the extension of methods of [1,2] to coupling with diffusion in the embedding space has not been published. Coupling to dynamics in the volume can be achieved by Monte Carlo type methods which were also used for simulating diffusive processes on surfaces [12,13]. This technique, however, has a slow convergence rate and requires an exact, analytically defined, surface.

In this paper, we present a numerical algorithm for solving Eq. (1) on arbitrary pixilated surfaces, which allows for coupling to a reaction–diffusion system in the volume within a fully conservative discretization scheme. Its development has been motivated by the need to include a capability of modeling surface diffusion in the Virtual Cell computational framework (VCell) [14], a general-purpose tool designed for experimental cell biologists (as well as theorists) to test their hypotheses and models. It allows a user to couple cellular chemical kinetics, diffusion–advection transport and electrophysiological properties of membranes into a system of time-dependent partial differential equations (PDEs) in two or three dimensions and solve the system numerically on

[1] Although this implies uniform D_i, the algorithm described in the paper is applicable to non-uniform D_i as well.

arbitrary geometry [15,16]. After extensive testing (a selection of tests is described in detail in Section 2.5 of part I), the proposed method has been incorporated into VCell and is now freely accessible at www.vcell.org.

Our algorithm, as detailed in part I, is relatively simple and performs at low computational cost. As an example, in the application of part II of this paper, a computation of 45 time steps performed on the grid of 10,830 surface and 96,390 volume mesh nodes yielding acceptable accuracy takes 85 s (all computations were performed on a Windows compute node with an Intel Xeon 2.8 GHz CPU); the same simulation on the grid of 97,504 surface and 2,438,920 volume nodes takes 86 min. In both cases, the computation time includes geometry processing and meshing. Consistently with the way VCell handles volume diffusion, Eq. (1) are discretized using a finite volume (area) scheme to guarantee mass conservation. The method applies to arbitrary pixilated surfaces inferred from segmented experimental images. This data format is familiar to cell biologists and can be obtained by accessible image processing tools. While the method neither requires nor produces an explicit smooth watertight surface, it allows the user to improve accuracy by refining the mesh as needed. In the example cited above, the relative error is estimated to be in the range of few percent, acceptable in biological applications for all practical purposes. Convergence studies in Sections 2.4 and 2.5 indicate an order of convergence in space between 1 and 2.

The paper consists of two parts. The key ideas of the method – to approximate LBO locally with the Laplacian on a tangential plane, and then apply a finite volume discretization scheme based on a Voronoi decomposition – are described in part I, along with the analysis of convergence and a representative selection of tests used to validate the algorithm. In part II, we present an application of the algorithm to a concrete cell-biological problem. The application involves modeling of fluorescence loss in photobleaching (FLIP) on realistic cell geometry in the situation where a signaling molecule called Rac cycles between the cell interior and the cell membrane, and therefore the surface diffusion of Rac is coupled to its diffusion in the cytoplasm. A simplified way of analyzing FLIP data was proposed in [17] to infer a rate of dissociation of Rac from the membrane. The modeling study presented here helps validate the procedure and assess its accuracy.

2. Part I. Numerical algorithm

2.1. Diffusion on a curved surface

Consider a volumetric domain Ω and assume that a regular orthogonal grid of size h is imposed on a box containing Ω. A pixilated approximation of Ω is given by Ω_h, the union of the volume elements with centers in Ω. The boundary of Ω_h is a stepwise surface S_h which is composed of rectangular facets with side length h, as illustrated in Fig. 1. The centers of these facets comprise a set of nodes $\{\mathbf{r}_i, i = 1, \ldots, N_S\} \subset R^3$ on S_h. These are the points at which jump conditions for volume PDEs and other membrane interactions are evaluated in VCell. For this reason, it is convenient to solve for the concentrations of membrane molecules at exactly the same points, because it facilitates coupling with the volume variables. Even though the points $\{\mathbf{r}_i\}$ do not

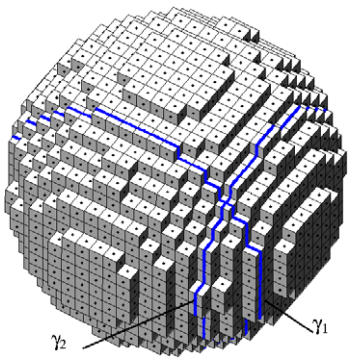

Fig. 1. A "staircase" approximation S_h of a sphere obtained by orthogonal meshing of the volume. Similar pixilated surfaces (stepwise curves in 2D) arise from microscope images. The centers of the staircase facets comprise a set of computational nodes on the surface. γ_1 and γ_2 are stepwise contours obtained by dissecting S_h in two Cartesian directions.

necessarily lie on S, our algorithm uses these points to approximate the solution of Eq. (1) on S. We utilize a finite volume discretization scheme, which is used frequently in transport problems and guarantees that numerical errors do not violate mass conservation [18].

Whereas the distances from the approximate nodes to the true surface converge to zero as h tends to zero, the surface area of S_h does not converge to the area of S, and neither do geodesic distances between nodes on S_h converge to geodesic arc lengths on S. To obtain a convergent solution to the PDE, our algorithm first calculates convergent approximations of the normals to the surface at the staircase points, and then uses them to approximate LBO locally by the Laplacian on a tangential plane.

Let $\mathbf{r}_i^{(S)}$ be the point in S that is closest to $\mathbf{r}_i$. If the locations of all points $\{\mathbf{r}_i^{(S)}\}$ were known and the geodesic distances between any pair of them could be computed, one could apply the finite volume method by partitioning the surface S into a set of surface elements $\{M_i\}$, each surrounding $\mathbf{r}_i^{(S)}$, and integrating Eq. (1) over each patch, i.e.

$$\frac{\partial}{\partial t}\int_{M_i} C\,\mathrm{d}A = \int_{\partial M_i} D\,\mathrm{grad}_S\, C\cdot\mathbf{n}\,\mathrm{d}s + \int_{M_i} R\,\mathrm{d}A, \quad i=1,\ldots,N_S, \tag{2}$$

where ∂M_i is the boundary of the ith surface element, and $\mathbf{n}$ is an outward normal to ∂M_i tangential to the surface (see Fig. 2) [19]. The index enumerating variables is omitted in Eq. (2) for simplicity. One way of partitioning S into regions $\{M_i\}$ is the Voronoi decomposition [20], in which the region M_i is comprised of all points on S that are closer to the i-th node than to any other node. The Voronoi decomposition is convenient for approximating the contour integral $\int_{\partial M_i}(\partial C/\partial n)\mathrm{d}s$ in Eq. (2) since the shared borders between adjacent Voronoi cells are always orthogonal to the geodesic curves connecting the nodes of these cells, and therefore, flux densities are easily approximated based on concentration values at the nodes and the arc length between nodes.

We apply a similar approach in the case of unknown $\mathbf{r}_i^{(S)}$ by integrating the equation on a set of locally planar Voronoi polygons centered at the approximate points $\{\mathbf{r}_i\}$. To construct these polygons, we first approximate the normal vector to S at each surface point $\mathbf{r}_i^{(S)}$ based on the known points $\{\mathbf{r}_i\}$ on S_h. For this, we consider contours γ_1 and γ_2 on two mutually orthogonal slices of S_h crossing at node $\mathbf{r}_i$, as shown in Fig. 1. In each slice, the tangent to the surface at point $\mathbf{r}_i^{(S)}$ is approximated by finite differences using two nearby nodes that are apart from $\mathbf{r}_i$ by k steps along the corresponding stepwise contour. The number of steps k is chosen in a way that guarantees convergence as $h\to 0$; it depends on local curvature and increases with decreasing mesh size. The fastest convergence to the correct tangents is achieved with $k=\mathrm{O}(h^{-q})$ where q, which is less than 1, depends on the particular method used for computing the tangent (see Appendix for details). Finally, the unit normal vector $\mathbf{N}_i$ at the i-th node is determined as the normalized cross-product of the two tangent vectors along both contours.

Once the normal $\mathbf{N}_i$ is computed, a polygon centered at $\mathbf{r}_i$ is constructed in the plane Π_i that is orthogonal to $\mathbf{N}_i$. A set of nodes in a certain neighborhood of $\mathbf{r}_i$ is projected onto Π_i. In the current implementation, this neighborhood includes all the nodes $\mathbf{r}_j$ whose corresponding facets have at least one common point with the facet of $\mathbf{r}_i$. The projections $\tilde{\mathbf{r}}_j=\mathbf{r}_j-\mathbf{N}_i(\mathbf{N}_i\cdot(\mathbf{r}_j-\mathbf{r}_i))$ and the point $\mathbf{r}_i$ form a set of co-planar points to which a two-dimensional Voronoi decomposition is applied [Qhull (www.qhull.org), a publicly available library, is used for this computation]. The procedure yields the natural neighbors of the node $\mathbf{r}_i$ and a polygon centered at the i-th node. Since $\mathbf{N}_i$ converges to the exact normal to the surface at $\mathbf{r}_i^{(S)}$, the planar Voronoi polygons constructed for the nodes $\mathbf{r}_i$ converge to the curved Voronoi cells centered around $\mathbf{r}_i^{(S)}$. The planar

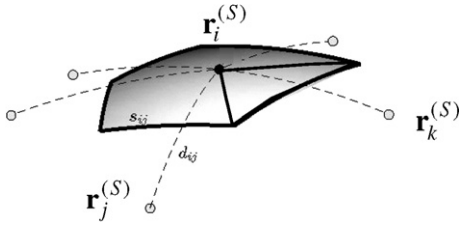

Fig. 2. A control area M_i with the boundary ∂M_i. Solid lines delineate a triangle Δ_{ik} referred to in Eq. (5).

distances between $\mathbf{r}_i$ and its projected neighbors approximate the geodesic distances d_{ij} between the corresponding points on S shown in Fig. 2, and the length of each side of the polygon approximates the geodesic length s_{ij}. Because the procedure does not automatically guarantee that $d_{ij} = d_{ji}$ and $s_{ij} = s_{ji}$, these quantities are symmetrized: $d_{ij}^{\text{sym}} = (d_{ij} + d_{ji})/2$ and $s_{ij}^{\text{sym}} = (s_{ij} + s_{ji})/2$. One can show that the order of convergence of d_{ij}^{sym} and s_{ij}^{sym} is the same as that of $\mathbf{N}_i$.

Eq. (2) is approximated on the new set of polygons as follows. The area of the i-th surface element, A_i, is approximated as $\frac{1}{4}\sum_{j\in G(i)} d_{ij}^{\text{sym}} s_{ij}^{\text{sym}}$. The expression $\sum_{j\in G(i)} D\frac{C_j - C_i}{d_{ij}^{\text{sym}}} \cdot s_{ij}^{\text{sym}}$ approximates the total diffusive flux entering the ith Voronoi cell, where $G(i)$ is the set of indexes enumerating Voronoi cells having common borders with the i-th cell (the natural neighbors of node i). Other terms of Eq. (2) are integrated over the area of a Voronoi cell using a first-order approximation, which yields the following spatial discretization of Eq. (1):

$$A_i \frac{\mathrm{d}C_i}{\mathrm{d}t} \approx \sum_{j\in G(i)} D\frac{C_j - C_i}{d_{ij}} \cdot s_{ij} + A_i R_i, \tag{3}$$

where from now on, d_{ij} and s_{ij} are used to designate d_{ij}^{sym} and s_{ij}^{sym} for simplicity. Mass conservation is easily verified by summing up Eq. (3) over all Voronoi cells. Partitioning into Voronoi polygons also facilitates mesh regularity, given a relatively uniform distribution of the nodes $\{\mathbf{r}_i\}$, which arises from the uniform meshing of the volume.

Eq. (3) is discretized in time using a first-order backward Euler scheme with an explicit treatment of the reaction term. Let C_i^{old} represent the computed solution at time t, and R_i^{old} be the reaction term evaluated at time t, then the solution C_i at time $t + \Delta t$ is found by solving:

$$A_i \frac{C_i - C_i^{\text{old}}}{\Delta t} = \sum_{j\in G(i)} D\frac{C_j - C_i}{d_{ij}} s_{ij} + A_i R_i^{\text{old}}. \tag{3a}$$

The resulting sparse linear system is solved iteratively using a preconditioned conjugate gradient method with an incomplete LU preconditioner.

In summary, our algorithm includes the following steps:

(i) find approximations for unit normals $\mathbf{N}_i$ at all computational nodes $\{\mathbf{r}_i, i = 1, \ldots, N_S\}$.
(ii) for each $\mathbf{r}_i$, find the orthogonal projections of its neighbors $\mathbf{r}_j$ onto the tangential plane, i.e. $\tilde{\mathbf{r}}_j = \mathbf{r}_j - \lambda \mathbf{N}_i$, where $\lambda = \mathbf{N}_i \cdot (\mathbf{r}_j - \mathbf{r}_i)$.
(iii) after computing a Voronoi decomposition for $\mathbf{r}_i$ and its neighbors' projections $\tilde{\mathbf{r}}_j$, find lengths d_{ij} and s_{ij}.
(iv) compute the symmetrized distances $d_{ij}^{\text{sym}} = (d_{ij} + d_{ji})/2$, $s_{ij}^{\text{sym}} = (s_{ij} + s_{ji})/2$ and the area $A_i = \frac{1}{4}\sum_{j\in G(i)} d_{ij}^{\text{sym}} s_{ij}^{\text{sym}}$; use these values in Eq. (3a).
(v) solve Eq. (3a) to advance the solution in time.

2.2. Coupling between surface and volume variables

The coupling of surface diffusion with a reaction–diffusion system in the volume is important in cell-biological applications where proteins diffusing inside the cell can bind to the membrane whereas membrane-bound proteins can dissociate and become free to diffuse in the cytoplasm (see part II for an example). Because in our method computational nodes on the surface arise from the meshing of a volumetric computational domain, it is relatively straightforward to couple membrane diffusion to the processes in the bulk. Still, care must be exercised to ensure full compatibility of the volume and surface solvers such that they preserve mass conservation.

To solve the reaction–diffusion equations in the volume, VCell utilizes a structured orthogonal grid [16]. This facilitates automatic sampling of cell geometry, particularly when it is based on experimental microscope images, where we can only tell whether a square pixel in the image lies inside or outside the cell, and also allows one to move easily from one-dimensional to two- to three-dimensional simulations. However, a 'staircase' approximation of a cell membrane that results from this kind of spatial discretization, in addition to problems discussed above in the context of surface diffusion, also creates difficulties for the accurate description of membrane fluxes, because the surface area of the 'staircase' does not converge to that of a real smooth

membrane when the mesh is refined. A "flux correction" method of effective smoothing [16] was adopted in the Virtual Cell to circumvent this problem.

Briefly, in the presence of the cell membrane S, a reaction–diffusion equation for a species concentration u, $u_t = \nabla(D\nabla u) + R$, where D is a diffusion coefficient and R is a reaction term, is subject to membrane jump conditions: $-(D\nabla u)_+\mathbf{N} = j_+, -(D\nabla u)_-\mathbf{N} = j_-$, where $\mathbf{N}$ is the outward normal to the membrane S, $+$ and $-$ denote the inside and outside of the cell, and j_+, j_- are inward and outward membrane flux densities that can be due to (un)binding processes as well as due to a cross-membrane flow (in the latter case, $j_+ = j_-$). Because the flux densities specified in the jump conditions are meant to be normal to the real membrane, the corrected (inward) flux density across the ith staircase membrane element is $j_+\cos\theta_i$ where θ_i is the angle between $\mathbf{N}$ and the normal to the ith staircase facet. Hence the corrected flux across this membrane element will be $j_+h^2\cos\theta_i$, where h^2 is the area of the staircase facet. In our practical implementation, it was the "corrected" area $a_i = h^2\cos\theta_i$ of the membrane element which was stored and used for calculating membrane fluxes. Because it is different from the Voronoi cell area A_i used to solve the surface reaction–diffusion equations (1), this inconsistency would obviously violate mass conservation when surface and volume variables are coupled.

Mass conserves automatically if the same surface area is used for evaluating membrane fluxes and reaction rates at the membrane. One possible strategy is a time-splitting approach where membrane variables are updated in two separate sub-steps, first due to diffusion and then due to reactions. This would allow one to keep the Voronoi areas A_i for the surface diffusion, whereas the corrected area a_i would be used for all other processes: membrane reactions, boundary fluxes etc. In an alternative approach, which avoids time-splitting, the Voronoi areas A_i are used for all purposes, including calculating membrane fluxes. This method tested for a coupled problem (see Section 2.5) yields an order of convergence between 1 and 2, same as for the surface diffusion alone. In addition, the test with the uncoupled volume diffusion shows that replacing a_i with A_i does not affect the order of convergence and in fact decreases the magnitude of the error. Therefore, this approach has been incorporated in the algorithm.

2.3. Boundary conditions

As mentioned above, in VCell, the domain of interest Ω is placed in a rectangular box. Solving Eq. (1) on a closed surface contained entirely in the box does not require boundary conditions. In the case of an open surface, which intersects with the walls of the box (such as the cylindrical surface of the test example in Section 2.5), boundary conditions need to be specified at the intersection, as either a given concentration, or normal flux. One problem with the open surface is that the standard Voronoi decomposition might not produce closed polygons for the nodes at the surface edge. Also, care must be exercised to ensure that the flux through the sides of the Voronoi polygons representing the edge of the surface is approximated correctly.

To close the polygons at the surface edge, temporary fictitious neighbors of the nodes at the boundary are added in a way that allows for the standard decomposition to be applied without any change. The flux boundary conditions are implemented in the spirit of the "flux correction" approach as described in Section 2.2 by taking into account that the flux enters the surface in the direction of the vector $\boldsymbol{\tau}\times\mathbf{N}_i$, where $\boldsymbol{\tau} = (\mathbf{N}_{\text{boundary}}\times\mathbf{N}_i)/|\mathbf{N}_{\text{boundary}}\times\mathbf{N}_i|$, with $\mathbf{N}_i$ and $\mathbf{N}_{\text{boundary}}$ being the outward normals to the surface at the i-th boundary node and to the box wall, respectively.

2.4. Convergence studies

Convergence of the numerical solution often follows from the local consistency of a discretization scheme. In applying our algorithm to surfaces approximated by a staircase, the sampling noise induces a divergent local truncation error as illustrated in Fig. 3 for diffusion on a sphere. Indeed, the local truncation error due to spatial discretization is given by $\tau_i = (D(\Delta_S - L_h)C)_i$ where C is the exact solution to the problem $C_t = D\Delta_S C$ and the operator L_h is defined as (see Eq. (3))

$$(L_hC)_i \equiv \frac{1}{A_i}\sum_{j\in G(i)}\frac{C_j - C_i}{d_{ij}}s_{ij}. \tag{4}$$

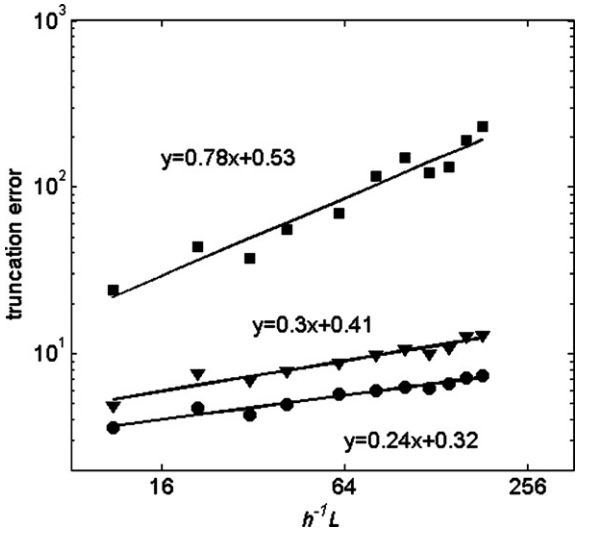

Fig. 3. Divergence of the truncation error for the sphere test problem (Section 2.5) in L_1 (circles), L_2 (triangles), and L_∞ (squares) norms. The local truncation error, calculated as $\tau = -DL_h C_{\text{exact}}(t+\Delta t) + (C_{\text{exact}}(t+\Delta t) - C_{\text{exact}}(t))/\Delta t$ with L_h defined in (4), is dominated, for sufficiently small Δt, by the truncation error due to spatial discretization, $D(\Delta_S - L_h)\, C_{\text{exact}}$. The results are obtained with $\Delta t = 10^{-4}$, small enough to ignore the effect of the time discretization error (see Section 2.5): $\|\tau\|_1 = O(h^{-0.2})$, $\|\tau\|_2 = O(h^{-0.3})$, and $\|\tau\|_{\infty=} = O(h^{-0.8})$.

The truncation error can be rewritten as $\tau_i = \frac{D}{A_i}\sum_{j\in G(i)}\eta_{ij}$ with

$$\eta_{ij} = \left(\frac{s_{ij}d_{ij}}{4}\Delta_S C_i - \int_{\Delta_{ij}} \Delta_S C \,\mathrm{d}A\right) + \left(\int_{\gamma_{ij}} \nabla_S C \cdot \mathbf{n}\,\mathrm{d}s - \frac{C_j - C_i}{d_{ij}} s_{ij}\right), \tag{5}$$

where Δ_{ij} is the triangle with base s_{ij} and node $\mathbf{r}_i$ (Fig. 2).

Because of the sampling noise, the error in distances s_{ij} and d_{ij} that enter Eq. (3) is $O(h^q)$ with $q < 1$ (see Appendix). It then follows from (5) that

$$\eta_{ij} \approx \int_{\gamma_{ij}} \nabla_S C \cdot \mathbf{n}\,\mathrm{d}s - \frac{C_j - C_i}{d_{ij}} s_{ij} = O(h^q) s_{ij} = O(h^{q+1}),$$

which leads to a diverging truncation error: $\tau_i = \frac{D}{A_i} O(h^{q+1}) = O(h^{q-1})$. Nevertheless, the solution converges with an order greater than 1, as illustrated in Fig. 4 for the sphere test problem and by other numerical tests in Section 2.5. Below we discuss the physics underlying this transformation.

Define the solution error $z = (C - C_h)$ where C_h is a finite volume approximation of the exact solution C obtained on a given set of computational nodes $\{\mathbf{r}_i\}_{i=1}^N$ by replacing Δ_S with the operator L_h. The solution error relates to the truncation error through the equation [18],

$$z_t = DL_h z + \tau. \tag{6}$$

The solution of Eq. (6) can be written as a convolution of the truncation error with a smooth non-negative Green's function ψ,

$$z_i(t) = \int_0^t \mathrm{d}t' \sum_j \psi_{ij}(t,t')\tau_j(t')A_j = \int_0^t \mathrm{d}t' D \sum_j \sum_{k\in G(j)} \eta_{jk}(t')\psi_{ij}(t,t'). \tag{7}$$

The terms summed in (7) are significantly non-zero in the region of the size $\sim\sqrt{Dt}$ centered at the i-th node. For $Dt \gg h^2$, the sum in (7) contains a large number of terms with alternating signs, which makes it possible for the solution error to become convergent.[2] One source of sign alternation is the flux consistency (mass

[2] For Dt less than or on the order of h^2, the error z is dominated by the smallness of time and is $t\tau_i$=$O(h^{q+1})$.

conservation) of the numerical scheme [21], $\eta_{jk} = -\eta_{kj}$, which results in gaining of at least one additional order of accuracy relative to the order of the truncation error [22]. In addition, the sign of η_{jk} alternates rapidly. These oscillations, which originate from the approximation of normals based on the staircase surface S_h, lead to an additional partial cancellation of the error. Our numerical experiments in 2D indicate that this cancellation results in a gain of another half an order of accuracy. We therefore conclude that the overall convergence in space is expected to be of the order greater than 1. Consistent with this conclusion, test results in the next section show convergence of the solution with an order between 1 and 2.

2.5. Numerical tests

A selection of numerical tests presented in this section illustrates the overall accuracy of the algorithm. In each test, a 3D box $[-L, L]^3$ containing a given analytical surface is meshed uniformly to produce an orthogonal grid with n^3 points and spatial step $h = 2L/(n-1)$. The diffusion coefficient in Eq. (1) is set to 1 and the equation is integrated over the time interval $[0, T]$ using a first-order backward Euler time discretization scheme. The resulting sparse linear system is solved by the GMRES iterative method with a preconditioner based on incomplete LU factorization. This is implemented by using PCGPAK (Scientific Computing Associates, New Haven, CT).

In this section, we are concerned with a spatial discretization error. To ensure its dominance in the overall error, the tests have been run with a sufficiently small fixed time step ($\Delta t = 10^{-4}$ was used in all the tests since a further reduction of the time step had a negligible effect on the total error; to illustrate a computational cost, a simulation of 1000 time steps for a sphere test problem (see below) run on an Intel Xeon 2.8 GHz node for the grid of 39,696 surface and 1,061,208 volume points takes 45 min of CPU time).

The following error norms are computed from the local errors $z_i = (C - C_h)_i$: $\|z\|_1 = \sum_i |z_i| A_i / \sum_i A_i$, $\|z\|_2 = (\sum_i z_i^2 A_i / \sum_i A_i)^{1/2}$, $\|z\|_\infty = \max |z_i|$. The corresponding relative errors, E_1, E_2, and E_∞ are computed by multiplying the norms by $1/\|C\|_2$.

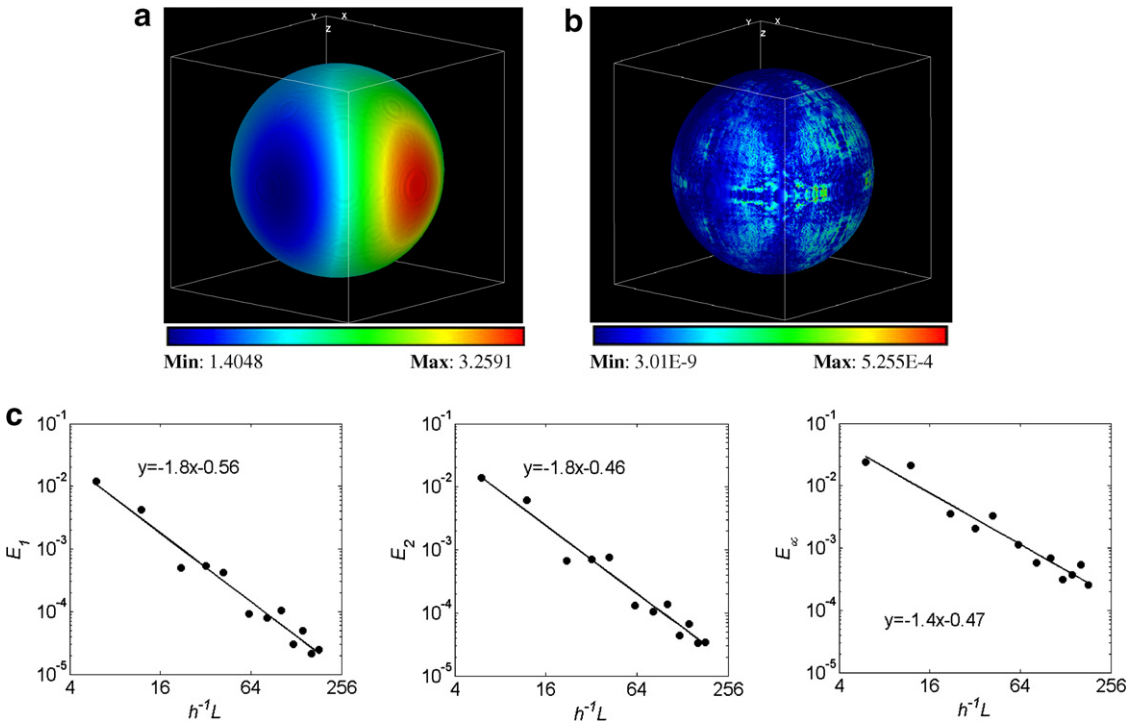

Fig. 4. Diffusion on a sphere: (a) numerical solution of the diffusion equation; (b) distribution of the absolute error of this solution for $T = 0.1$ obtained with $h = 0.012$ and $\Delta t = 10^{-4}$; (c) relative error as a function of h in L_1, L_2, and L_∞ norms, respectively.

2.5.1. Diffusion on a sphere

In this example, the algorithm is tested against an exact solution on a sphere of radius 1. In the case of one variable and no source term, a general solution of Eq. (1), which in spherical coordinates $\{\theta, \psi\}$ takes the form

$$\frac{\partial C}{\partial t} = \frac{1}{\sin\theta}\frac{\partial}{\partial\theta}\left(\sin\theta\frac{\partial C}{\partial\theta}\right) + \frac{1}{\sin^2\theta}\frac{\partial^2 C}{\partial\psi^2},$$

is $C(\theta,\psi,t) = \sum_{n=0}^{\infty}\sum_{m=0}^{n} e^{-n(n+1)t}(a_{n,m}\cos n\psi + b_{n,m}\sin n\psi)P_n^m(\cos\theta)$, where $P_n^m(\cos\theta)$ are the associated Legendre polynomials. Several low-order terms are used to construct an asymmetrical solution,

$$C(\theta,\psi,t) = 2 + 0.5e^{-2t}\cos\psi\sin\theta + e^{-6t}\cos 2\psi\sin^2\theta + e^{-12t}\cos 3\psi\sin^3\theta.$$

Fig. 4a shows the solution obtained on a $182\times182\times182$ grid ($L = 2.2$, $h = 0.012$) at $T = 0.1$. The corresponding error distribution and the relative error plots are shown in Fig. 4b and c, respectively.

2.5.2. Diffusion on a surface of revolution with varying curvature

It is generally true that biological applications involve domains with irregular shapes. This test is designed to study how well the algorithm performs on a surface with varying curvature. The idea is to use a surface of revolution and axisymmetric initial conditions to recast the problem into an equivalent one-dimensional diffusion–advection problem. The algorithm is then tested against a highly accurate numerical solution of the equivalent 1D problem which is regarded as "exact".

Let S be a closed surface obtained by revolving a given smooth curve around the z-axis in R^3. The surface is parametrized by two normal coordinates: s, the length of a geodesic line along a meridian from one of the poles on the z-axis, and ψ, the angular coordinate along the parallel. S is then defined by $r = r(s)$ where r is the distance between the point on the surface and the axis of symmetry (a radial coordinate), and the axisymmetric (i.e. independent of ψ) diffusion on S is described by a one-dimensional PDE, $\frac{\partial C}{\partial t} = \frac{1}{r(s)}\frac{\partial}{\partial s}\left(r(s)\frac{\partial C}{\partial s}\right)$.

If the curve used to obtain S is defined in polar coordinates ρ and θ, so that $z = \rho(\theta)\cos\theta$ and $r = \rho(\theta)\sin\theta$, then equation above becomes

$$\frac{\partial C}{\partial t} = \frac{1}{r(\theta)s'(\theta)}\frac{\partial}{\partial\theta}\left(\frac{r(\theta)}{s'(\theta)}\frac{\partial C}{\partial\theta}\right),$$

where $C \equiv C(\theta,t)$ and $s'(\theta) = \sqrt{\rho^2 + (\rho')^2}$. The surface used in the test is produced by revolving the curve $\rho(\theta) = 1.5 - 0.5\cos(8\theta)$, and the size of the box is $L = 2$. The "exact" solution is obtained with the initial conditions $C(\theta,0) = \begin{cases} 1, & \theta\in[0,\pi/2] \\ 0, & \theta\in(\pi/2,\pi] \end{cases}$ and shown in Fig. 5 for $T = 5$ along with the spatial error distribution and the corresponding convergence plots.

2.5.3. Diffusion on a cylinder (open surface)

Unlike the previous examples which involve closed surfaces, this test deals with the case of an open surface intersecting the walls of the box where boundary conditions need to be specified. In VCell, either a given concentration (Dirichlet boundary conditions) or normal flux density (Neumann boundary conditions) are accommodated. In this test, zero flux boundary conditions are imposed on a circular cylinder of radius 1 placed in a box of size $L = 1.5$. The cylinder is parametrized as $x(\theta,\xi) = \xi$, $y(\theta,\xi) = \cos\theta$, $z(\theta,\xi) = \sin\theta$ for $-L \leqslant \xi \leqslant L$ and $-\pi \leqslant \theta < \pi$. With this parametrization, the surface diffusion equation takes the form, $\frac{\partial C}{\partial t} = \frac{\partial}{\partial\theta}\left(\frac{\partial C}{\partial\theta}\right) + \frac{\partial}{\partial\xi}\left(\frac{\partial C}{\partial\xi}\right)$, and the exact solution used in the test is given by $C(\xi,\theta,t) = e^{-(\pi^2+1)t}\cdot\sin\pi\xi\cdot\sin\theta$. The results obtained for this test problem are illustrated in Fig. 6.

2.5.4. Coupling of diffusion on a sphere with diffusion in the volume

Here we study how the coupling of surface (C_S) and volume (C_V) variables affects accuracy of the algorithm. The test is performed against an exact solution of a system of two coupled PDEs,

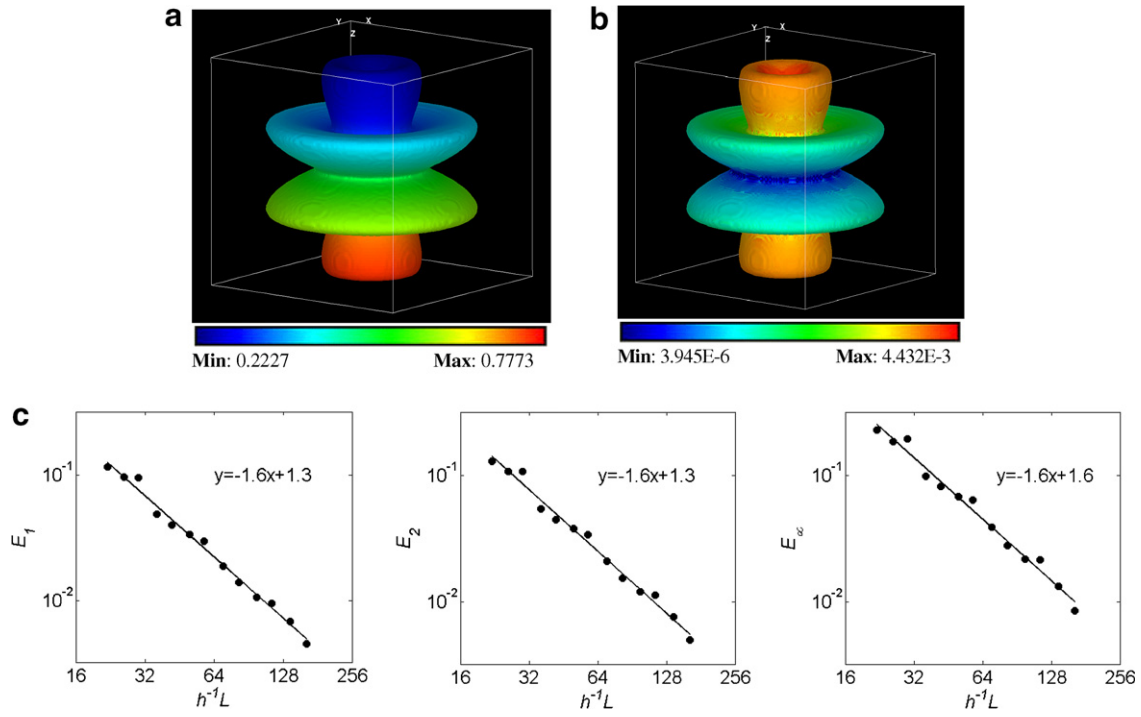

Fig. 5. Diffusion on a surface of revolution: (a) numerical solution of the diffusion equation obtained at $T = 5$ with $h = 0.025$ and $\Delta t = 10^{-4}$; (b) corresponding distribution of the absolute error; (c) relative error as a function of h in L_1, L_2, and L_∞ norms, respectively.

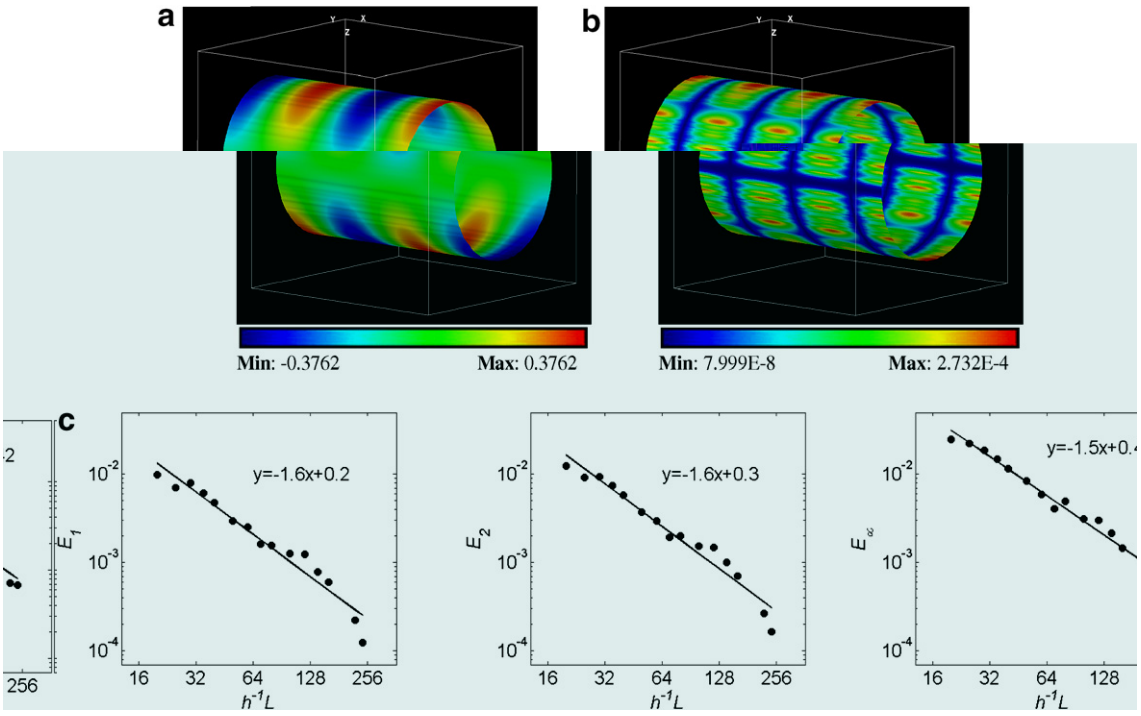

Fig. 6. Diffusion on a cylindrical surface: (a) numerical solution of the diffusion equation obtained at $T = 0.1$ with $h = 0.019$ and $\Delta t = 10^{-4}$; (b) corresponding distribution of the absolute error; (c) relative error as a function of h in L_1, L_2, and L_∞ norms, respectively.

$$\frac{\partial C_V}{\partial t} = \Delta C_V,$$
$$\frac{\partial C_S}{\partial t} = \Delta_S C_S + C_V|_{\partial\Omega} - C_S,$$

where $\partial\Omega$ is a sphere with radius 1, and the first (volume) equation is subject to the membrane jump condition: $-\mathbf{N}\nabla C_V|_{d\Omega} = C_S - C_V|_{\partial\Omega}$ where $\mathbf{N}$ is the outward normal. The system describes a molecular species that can diffuse in the volume, bind to, and dissociate from, the membrane, and once bound to the surface can undergo surface diffusion.

The search for an analytical solution is facilitated by using spherical coordinates ρ, θ and ψ,

$$\frac{\partial C_V}{\partial t} = \frac{1}{\rho^2}\frac{\partial}{\partial \rho}\left(\rho^2 \frac{\partial C_V}{\partial \rho}\right) + \frac{1}{\rho^2}\Delta_S C_V,$$
$$\frac{\partial C_S}{\partial t} = \Delta_S C_S + C_V|_{\rho=1} - C_S,$$

where $\Delta_S = \frac{1}{\sin\theta}\frac{\partial}{\partial\theta}\left(\sin\theta\frac{\partial}{\partial\theta}\right) + \frac{1}{\sin^2\theta}\frac{\partial^2}{\partial\psi^2}$, and $(\partial C_V/\partial\rho)|_{\rho=1} = C_S - C_V|_{\rho=1}$, and by seeking the solution in the form $C_V = f(\rho)C_S$. The following exact solution has been used in the test:

$$C_S(\theta,\psi,t) = A e^{-k^2 t}\cos\theta$$
$$C_V(\rho,\theta,\psi,t) = e^{-k^2 t}\left(\frac{\sin(k\rho)}{(k\rho)^2} - \frac{\cos(k\rho)}{(k\rho)}\right)\cos\theta,$$

with $A = \sin k + \frac{\cos k}{k} - \frac{\sin k}{k^2}$ and $k = 1.527338738$. The convergence of the numerical solution is illustrated in Fig. 7.

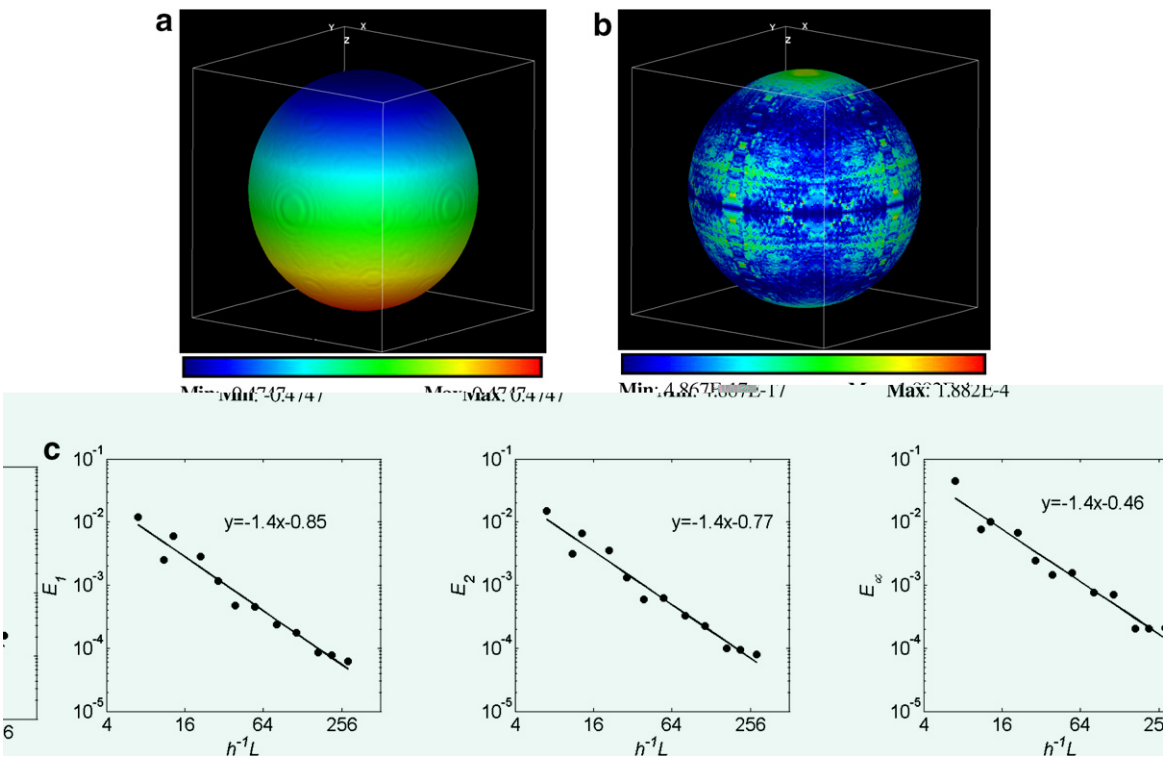

Fig. 7. Diffusion on a sphere coupled to diffusion in the volume: (a) numerical solution for the surface variable obtained at $T = 0.1$ with $h = 0.014$ and $\Delta t = 10^{-4}$; (b) distribution of the absolute error for this solution; (c) corresponding relative error as a function of h in L_1, L_2, and L_∞ norms, respectively.

3. Part II. Application to cell biology

3.1. Biological background and methods

In this section, we describe a cell-biological application which involves realistic 3D modeling of membrane diffusion coupled to diffusion in the cytosol. The problem concerns a small mobile protein Rac implicated in a number of processes including regulation of the actin cytoskeleton and cell migration. This protein exists both in the cytosol and cell membrane [23,24]. Binding to the membrane correlates with Rac activation and initiation of downstream signaling, whereas cytosolic Rac is thought to be mainly inactive. The processes that mediate Rac activation and binding to the membrane constitute an area of active research. In a recent study [17], a method of estimating parameters of the *in vivo* Rac binding to the membrane was proposed. In this method, measurements of fluorescence loss in photobleaching (FLIP) were analyzed with a non-spatial (compartmental) model. Based on this model, a simple fitting procedure was designed to estimate parameters of the Rac interaction with the membrane. Here, realistic simulations are used for validating the procedure and assessing the accuracy of the method.

In the experiments[3] [17], cells (NIH3T3 fibroblasts) were transfected with a genetic material encoding synthesis of Rac fused to a green fluorescent protein, GFP-Rac. The FLIP protocol was then applied, which involves continuous bleaching of GFP-Rac by a laser beam everywhere in the cell except for the small masked region at cell periphery. Simultaneously, fluorescence loss was recorded in the bleached and unbleached regions using a confocal microscope. A schematic of the experimental setup and a sample of typical experimental data are shown in Fig. 8 (courtesy of Kostas Moissoglu and Martin Schwartz). Although measurements in both regions were made in the same focal layer, the profiles of cell geometry (Fig. 9) were such that the signal in the bleached region came mainly from the cytosol whereas the fluorescence intensity recorded in the masked region was a mixture of signals from the unbleached membrane and cytosol. There are two processes contributing to the signal decay in the unbleached area: membrane diffusion of Rac and dissociation of Rac from the membrane followed by diffusion in the cytosol to the bleached region.

To obtain an estimate of the dissociation rate from the FLIP data, a simple two-step fitting procedure was designed based on the following observations: (i) in all experiments, the signal decay in the bleached region was fitted well (within a few-percent error) to a two-exponential function; (ii) loss of fluorescence from the unbleached membrane caused by the membrane diffusion alone is described well by a single exponential function [17]; (iii) the cytosolic diffusion of Rac over the width of the unbleached region is assumed to be much faster than interaction with the membrane and photobleaching. Based on the latter assumption, one can apply a compartmental approximation and introduce the surface density of GFP-Rac in the unbleached membrane domain, c_1, and the concentration of fluorescent GFP-Rac in the bleached cytosol, c_2.

First, based on observation (i), the normalized fluorescence decay in the bleached region was fitted to a two-exponential function:

$$c_{2,\mathrm{norm}} = \frac{c_2(t)}{c_2(0)} = a\exp(-\alpha t) + b\exp(-\beta t) \tag{8}$$

by varying parameters a, b, α, β constrained by $a, b, \alpha, \beta > 0$ and $a + b = 1$. At the second step, the normalized fluorescence in the unbleached area was fitted to a three-exponential function. This function is derived (see *Supplementary Text* in [17] for derivation details) by taking into account that both the membrane and cytosol contribute to the signal in the unbleached region. Denoting the unbleached membrane area and cytosol volume that contribute to the signal by s and v, respectively, one obtains $c_{\mathrm{unbleached,norm}}(t) = rc_{1,\mathrm{norm}}(t) + (1-r)c_{2,\mathrm{norm}}(t)$ where $c_{1,\mathrm{norm}}(t) = c_1(t)/c_1(0)$ and the additional parameter $r = s(s + vc_2(0)/c_1(0))^{-1}$ ranges from 0 at $s = 0$ (all the signal comes from the cytosol) to 1 at $v = 0$ (the signal comes solely from the membrane). In the compartmental approximation, c_1 is described by the equation $\mathrm{d}c_1/\mathrm{d}t = -(k_{\mathrm{off}} + k_{\mathrm{diff}})c_1 + k_{\mathrm{on}}c_2$ with k_{on}, k_{off} standing

[3] The idea and design of the experiments belong to K. Moissoglu and M. Schwartz; the experiments were performed by K. Moissoglu in Schwartz' laboratory, U. Virginia.

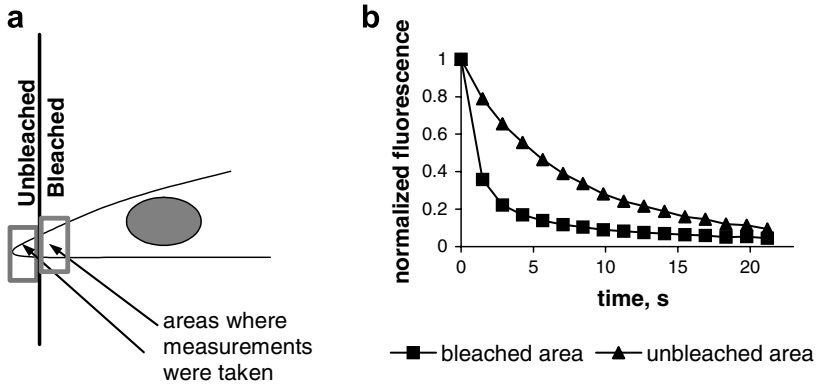

Fig. 8. Experimental setup and typical data (courtesy of K. Moissoglu and M. Schwartz): (a) a schematic of the experimental setup; (b) a typical sample of the experimental data.

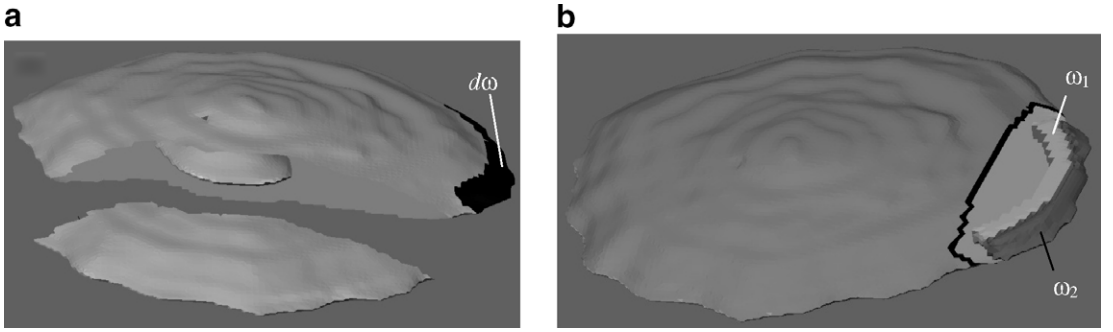

Fig. 9. Cell geometry and regions of interest: (a) cell geometry built from the stack of segmented confocal images of X–Y slices (smoothing is applied for visualization purposes only using the method of [25]); the nucleus is treated as excluded volume; the unbleached portion of the membrane dω (mask) is shown in black; (b) the cytosolic volume ω_1 in the bleached area from which fluorescence is "measured" is shown in white; the dark gray region is the unbleached cytosolic volume ω_2 under the mask, which contributes to the signal in the unbleached area.

for membrane association and dissociation rate constants, respectively, and k_{diff} being a rate of decay caused by Rac membrane diffusion alone. Using (8), this equation is readily solved to yield

$$c_{1,\text{norm}}(t) = \mathrm{e}^{-\gamma t} + (\gamma - k_{\text{diff}})(a(\gamma-\alpha)(\mathrm{e}^{-\alpha t} - \mathrm{e}^{-\gamma t}) + b(\gamma-\beta)(\mathrm{e}^{-\beta t} - \mathrm{e}^{-\gamma t}))$$

where $\gamma = k_{\text{off}} + k_{\text{diff}}$ (it is also taken into account that initially $\mathrm{d}c_1/\mathrm{d}t = 0$ and $k_{\text{diff}} = 0$ because the system is at equilibrium before photobleaching).

By taking all of the above into account, one arrives at the function,

$$c_{\text{unbleached,norm}}(t) = \tilde{a}\mathrm{e}^{-\alpha t} + \tilde{b}\mathrm{e}^{-\beta} t + \tilde{c}\mathrm{e}^{-\gamma t} \tag{9}$$

where $\tilde{a} = a(1 + r\frac{\alpha - k_{\text{diff}}}{\gamma-\alpha}), \tilde{b} = b(1 + r\frac{\beta - k_{\text{diff}}}{\gamma-\beta}), \tilde{c} = r(1 - a\frac{\gamma-k_{\text{diff}}}{\gamma-\alpha} - b\frac{\gamma-k_{\text{diff}}}{\gamma-\beta})$, that was used at the second step to fit the normalized fluorescence in the unbleached area by varying parameters γ and r in the range $\gamma > 0$ and $0 < r < 1$; at this step, parameters a, b, α, β were kept constant at values obtained from the initial fitting of the signal in the bleached region to Eq. (8). Parameter k_{off} was then determined as $k_{\text{off}} = \gamma - k_{\text{diff}}$ with k_{diff} estimated in a separate experiment [17]. Parameter r can be viewed as a qualitative indicator of the fraction of the membrane-bound Rac $r_0 = S(S + Vc_2(0)/c_1(0))^{-1}$ (V and S are the cytosol volume and membrane area, respectively), which is however quantitatively different from r. Note that if a local surface-to-volume ratio of the unbleached region, $\sigma = s/v$, is known, one can back calculate the ratio $k_{\text{off}}/k_{\text{on}}$ from parameter r, $k_{\text{off}}/k_{\text{on}} = \sigma(1-r)/r$, and thus estimate k_{on}.

3.2. 3D model and computations

To validate the method outlined in Section 3.1, a full spatial model is solved using the algorithm described in Part I of this paper. The idea is to model realistically both the experimental conditions and data collection. For given k_{off} and r, 3D simulations are used to generate "data". One can then subject the "data" to the fitting procedure as described above to see how close the recovered parameter estimates are to the values built in the model. Of particular interest is the extent to which the assumption of fast diffusion of Rac in the cytosol affects the accuracy of parameter estimates.

The model is formulated in terms of a spatiotemporal distribution of the surface density of GFP-Rac, $c_1(\mathbf{x},t)$, in the cell membrane $\mathrm{d}\Omega$ and the GFP-Rac concentration, $c_2(\mathbf{x},t)$, in the cytosol Ω. It is important to solve the problem on realistic cell geometry taken from experimental images[4] in order to mimic faithfully the data collection and to account for inhomogeneity of bleaching in z-direction and for the effect of the excluded volume of the nucleus. The simulated cell (Fig. 9) with the cytosol volume $V = 16{,}051\ \mu\text{m}^3$ and the plasma membrane surface area $S = 8407\ \mu\text{m}^2$ was placed in a 3D computational domain, $(0,L_x)\times(0,L_y)\times(0,L_z)$, with $L_x = 83.49\ \mu\text{m}$, $L_y = 79.65\ \mu\text{m}$, and $L_z = 9.5\ \mu\text{m}$.

Governing equations of the model are:

$$\begin{aligned}\frac{\partial c_1}{\partial t} &= D_1\Delta_S c_1 + R_{1,\text{bleach}} + R_{\text{bind}},\\ \frac{\partial c_2}{\partial t} &= D_2\Delta c_2 + R_{2,\text{bleach}}\end{aligned} \tag{10}$$

and the boundary condition for the variable c_2 is $D_2(\partial c_2/\partial N)|_{\mathrm{d}\Omega} = R_{\text{bind}}$ where $\mathbf{N}$ is the outward normal. No boundary conditions are needed for c_1 because $\mathrm{d}\Omega$ is closed. In Eq. (10), D_1 and D_2 are the diffusion coefficients in the membrane and in the cytosol, respectively. The first equation is defined only for $\mathbf{x}\in\mathrm{d}\Omega$ and Δ_S is the Laplace–Beltrami operator as defined in Part I of the paper.

The rates of photobleaching are $R_{i,\text{bleach}} = -V(\mathbf{x})c_i(\mathbf{x},t), i = 1,2$, where the spatially dependent rate constant $V(\mathbf{x}) = V_{\max}f(z)(1-\Theta(x,y))$ accounts for the inhomogeneity of photobleaching performed with a confocal microscope, $f(z) = h^2/(h^2+z^2)$, and mimics shielding of the unbleached region: $\Theta(x,y)$ equals 1 for the points under the mask and zero otherwise. In simulations, $V_{\max} = 1\ \text{s}^{-1}$, $h = 3\ \mu\text{m}$ and the masked region is shown in Fig. 9. The rate of binding to the membrane, which enters the first equation in (10) and the boundary condition for c_2, is $R_{\text{bind}} = -k_{\text{off}}c_1(\mathbf{x},t) + k_{\text{on}}c_2(\mathbf{x},t)$ where $\mathbf{x}\in\mathrm{d}\Omega$.

Before bleaching, the system is in equilibrium, and the initial distributions are uniform: $c_1(\mathbf{x},0)\equiv c_1(0)$, $c_2(\mathbf{x},0)\equiv c_2(0)$. It is convenient to introduce the ratio q of the number of membrane-bound Rac molecules and the number of Rac molecules in the cytosol, $q = r_0/(1-r_0)$, then $c_1(0)/c_2(0) = qV/S$ and $k_{\text{on}} = k_{\text{off}}S/qV$. The algorithm used to solve the model (10) numerically on the geometry of Fig. 9 utilizes uniform orthogonal meshing as described in part I of the paper. Simulations have been run with a 0.05-s time step on 96,390 volume grid points and 10,830 surface grid points. Average numerical error of $c_1(\mathbf{x},t)$ and $c_2(\mathbf{x},t)$ is estimated to be within 2–4%.

As in real experiments, we first estimate k_{diff} for a particular mask size (arc length 42 μm, average width 4 μm) used in simulations. For this, the first equation in (10) has been solved separately with $R_{\text{bind}} = 0$ and $D_1 = 0.25\ \mu\text{m}^2/\text{s}$ (in real experiments, a special molecular construct that does not dissociate from the membrane and has diffusive properties similar to those of Rac was used [17]). The normalized fluorescence in the unbleached portion of the membrane $\mathrm{d}\omega$ (Fig. 9) is $s^{-1}\iint_{\mathrm{d}\omega} c_1(\mathbf{x},t)/c_1(0)\mathrm{d}^2\mathbf{x}$ where $s = \iint_{\mathrm{d}\omega}\mathrm{d}^2\mathbf{x}$. Fitting to a one-exponential function yields $k_{\text{diff}} = 0.0352\ \text{s}^{-1}$ (Fig. 10).

The FLIP experimental protocol was then simulated by solving the full model (10) with parameters k_{off} and q, representative of those obtained in the experiments [17], and values of D_2 around 20 $\mu\text{m}^2/\text{s}$. This is an appropriate range for the diffusion coefficient of a cytosolic protein of the GFP-Rac size (~50 kDa), according to estimates and recent measurements [26]. The normalized fluorescence acquired from the portion of the bleached region ω_1 (Fig. 9), proximal to the unbleached domain, is calculated as $I_1(t) = v_1^{-1}\iiint_{\omega_1} c_2(\mathbf{x},t)/c_2(0)\mathrm{d}^3\mathbf{x}$ where $v_1 = \iiint_{\omega_1}\mathrm{d}^3\mathbf{x}$. The normalized signal recorded from the unbleached region (ω_2 and $\mathrm{d}\omega$) is modeled as

[4] The images were provided by K. Moissoglu and M. Schwartz, U. Virginia.

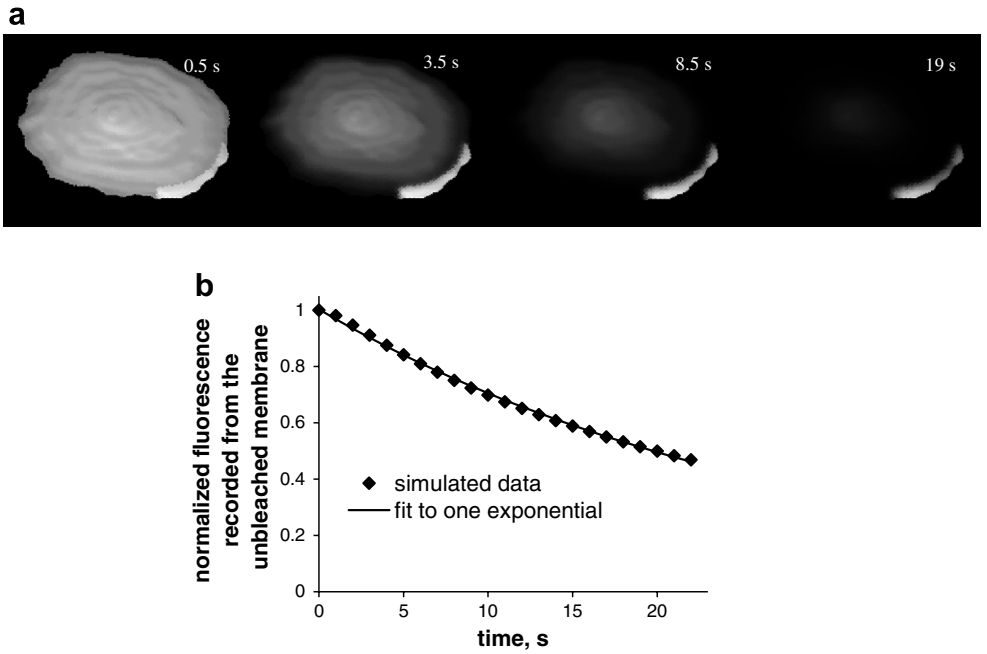

Fig. 10. Signal decay in the unbleached membrane in the case of a protein that does not dissociate from the membrane: (a) a series of snapshots from a simulation with the mask arc length of 42 μm and the average width 4 μm ($V_{max} = 1\ s^{-1}$, $h = 3$ μm, $D_1 = 0.25\ \mu m^2/s$); (b) normalized fluorescence recorded in the masked region of the membrane $d\omega$ is fitted to a one exponential function $A\exp(-k_{diff}t)$ with $k_{diff} = 0.0352\ s^{-1}$.

$$I_2(t) = (c_1(0)s + c_2(0)v_2)^{-1}\left(\int\int_{d\omega} c_1(\mathbf{x},t)d^2\mathbf{x} + \int\int\int_{\omega_2} c_2(\mathbf{x},t)d^3\mathbf{x}\right)$$

where $v_2 = \iiint_{\omega_2} d^3\mathbf{x}$. For the mask used in the simulations, $s = 151\ \mu m^2$ and $v_2 = 182\ \mu m^3$. Finally, the fitting procedure is applied to $I_1(t)$ and $I_2(t)$ as described above to obtain estimates of k_{off} and $r = (1 + v_2S/Vsq)^{-1} = (1 + 0.6313/q)^{-1}$. These estimates are then compared with values built in the model.

3.3. Results

A series of numerical experiments have been performed for all permutations of the parameter values: $k_{off} = 0.03, 0.05, 0.07\ (s^{-1})$, $q = 0.4, 1.0, 2.5$ (the corresponding r's are 0.387, 0.612, 0.798), which are representative of ranges typically observed in the experiments, and the following values of the diffusion coefficient in the cytosol: $D_2 = 10, 15, 20, 25, 30\ (\mu m^2/s)$. Interestingly, as in the real experiments, the simulated normalized signal in the bleached region, $I_1(t)$, was fitted well (within 1–2% error) to the two-exponential function in all cases, see Fig. 11, which illustrates the simulation outcome and results of the fitting in the case of $k_{off} = 0.05$, $q = 1.0$ ($r = 0.612$) and $D_2 = 20\ \mu m^2/s$.

The results of all simulations are summarized in Fig. 12 (and in Table 1) where each pair of recovered estimates of k_{off} and r is represented by a point in a two-dimensional parameter space. A symbol of the point indicates a particular value of the diffusion coefficient D_2 for which those estimates were obtained as described in the figure legend. The figure also includes the points (shown as filled diamonds) that represent the "true" parameters values listed above, so that a deviation from these points indicates how accurate the estimates are.

As expected, the recovered parameters tend to converge to the "true" values as diffusion in the cytosol becomes faster, and even in the case of slow diffusion, the estimates of k_{off} and r qualitatively follow the real values for any given D_2. Quantitatively, however, k_{off} is significantly underestimated in the case of high-affinity binding to the membrane (large q and r). This is because tight binding effectively slows down diffusion in the cytosol (similar effects are discussed in [27,28]). Not surprisingly, the estimate is skewed most of all when the

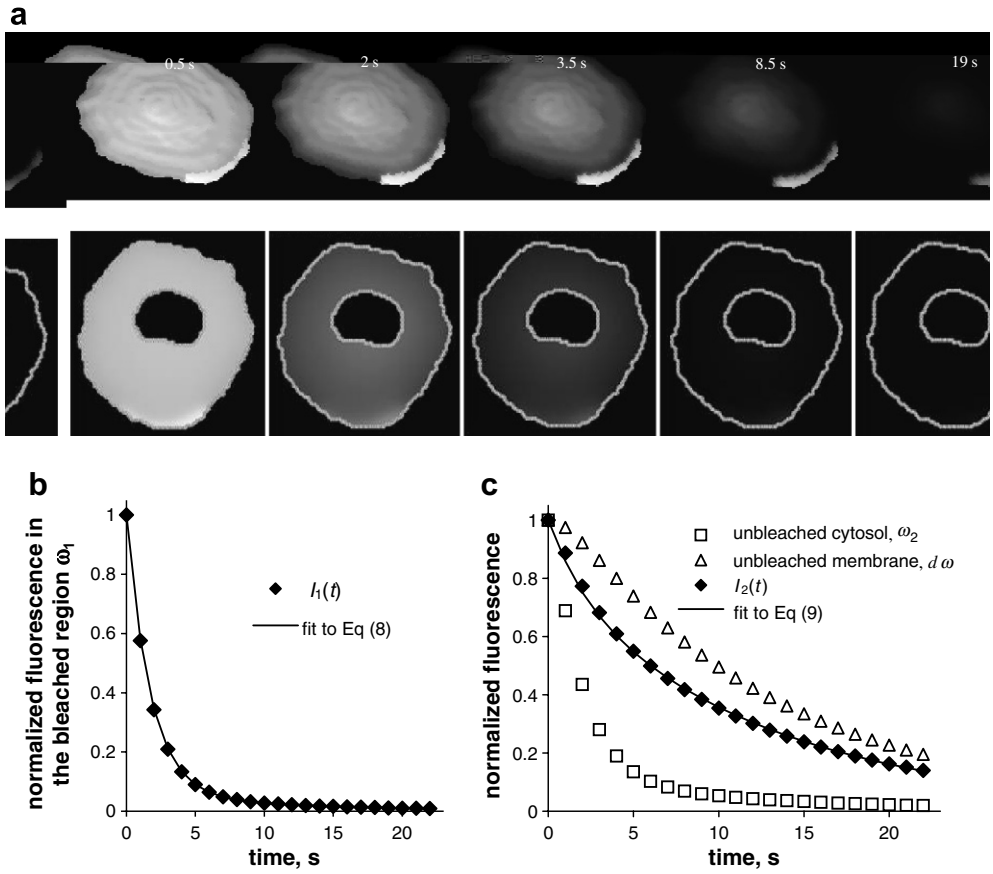

Fig. 11. Simulated "data" and an outcome of fitting for a representative parameter set: (a) a series of snapshots of fluorescence distribution in the membrane (top panel) and in the confocal z-slice ($0 < z < h$) inside the cell (bottom panel) from the FLIP simulation with $k_{\text{off}} = 0.05\ \text{s}^{-1}$, $q = 1.0$ ($r = 0.612$) and $D_2 = 20\ \mu\text{m}^2/\text{s}$; (b) normalized fluorescence $I_1(t)$ is recorded in the bleached region ω_1 and fitted to a two-exponential function, Eq. (8), with $\alpha = 0.5786\ \text{s}^{-1}$, $\beta = 0.0855\ \text{s}^{-1}$, $a = 0.94$ and $b = 0.06$; (c) normalized signals from the unbleached membrane $d\omega$ and the unbleached cytosol ω_2; the overall normalized fluorescence $I_2(t)$ is fitted to a three-exponential function, Eq. (9), to recover the estimates $k_{\text{off}} \approx 0.0474\ \text{s}^{-1}$ and $q \approx 1.18$ ($r \approx 0.652$).

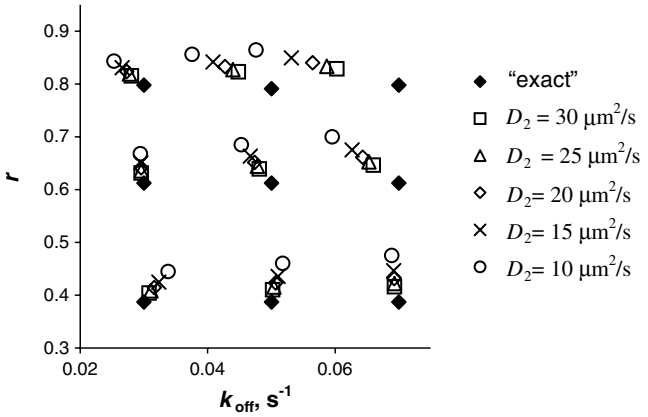

Fig. 12. Summary of results mapped onto the (k_{off}, r) parameter space.

Table 1
Estimates of parameter sets (k_{off}, r) recovered by the fitting procedure for various "exact" sets of values and cytosol diffusion constants as shown in Fig. 12

"Exact" sets (k_{off}, s^{-1}; r)	$D_2 = 30\ \mu m^2/s$	$D_2 = 25\ \mu m^2/s$	$D_2 = 20\ \mu m^2/s$	$D_2 = 15\ \mu m^2/s$	$D_2 = 10\ \mu m^2/s$
(0.03, 0.387)	(0.0308, 0.404)	(0.0311, 0.408)	(0.0316, 0.415)	(0.0323, 0.425)	(0.0338, 0.445)
(0.03, 0.612)	(0.0295, 0.631)	(0.0295, 0.635)	(0.0296, 0.641)	(0.0295, 0.651)	(0.0295, 0.668)
(0.03, 0.798)	(0.0280, 0.816)	(0.0277, 0.819)	(0.0273, 0.824)	(0.0266, 0.831)	(0.0253, 0.843)
(0.05, 0.387)	(0.0502, 0.410)	(0.0504, 0.415)	(0.0507, 0.423)	(0.0511, 0.435)	(0.0517, 0.460)
(0.05, 0.612)	(0.0481, 0.639)	(0.0478, 0.644)	(0.0474, 0.652)	(0.0467, 0.664)	(0.0453 0.685)
(0.05, 0.791)	(0.0448, 0.823)	(0.0439, 0.827)	(0.0427, 0.833)	(0.0408, 0.842)	(0.0375, 0.856)
(0.07, 0.387)	(0.0693, 0.416)	(0.0693, 0.422)	(0.0693, 0.431)	(0.0692, 0.446)	(0.0689, 0.475)
(0.07, 0.612)	(0.0660, 0.646)	(0.0653, 0.654)	(0.0643, 0.661)	(0.0627, 0.675)	(0.0596, 0.700)
(0.07, 0.798)	(0.0603, 0.829)	(0.0587, 0.834)	(0.0565, 0.840)	(0.0531, 0.849)	(0.0476, 0.864)

high-affinity binding is combined with large k_{off} because this case is the exact opposite of the situation where the cytosolic diffusion is fast compared to the rate of unbinding. Conversely, the estimates of k_{off} are more precise at low-affinity binding to the membrane (small q, r). Note that the "direction", in which the estimate deviates from the true value, rotates as $q(r)$ decreases so that the method tends to overestimate k_{off} in the "corner" of small k_{off} and $q(r)$. Unlike k_{off}, the values of parameter r are always overestimated by the method with the least relative error obtained in the large k_{off} – large q (r) "corner" of the parameter space.

These observations are important for a correct interpretation of results obtained from the analysis of the FLIP data with the method of [17]. As an example, consider two Rac mutants that have the same unbinding rate around $0.07\ s^{-1}$ but different binding affinities corresponding to r values of 0.4 and 0.8. According to Fig. 12, the fitting procedure can recover an estimate of k_{off} at $r = 0.8$ of up to 30% (at $D_2 = 10\ \mu m^2/s$) smaller than that at $r = 0.4$. The results in Fig. 12 therefore give an idea of a systematic error caused by the assumption of fast diffusion. Using this approach, one can create a table of systematic errors of the method, similar to Table 1, for comparing any two mutants with various binding affinities.

4. Concluding remarks

In this paper, we described and analyzed an algorithm for simulating diffusion on a curved surface, coupled to diffusion in the embedding space. The method is implemented within the Virtual Cell, a general-purpose tool for modeling cell-biological phenomena, thus adding a capability of modeling membrane diffusion coupled to processes inside and outside the cell. The method applies to arbitrary geometries obtained from experimental images. The image processing step is not a part of the algorithm. This separation from fully automated steps, such as geometry meshing and numerical solvers, is important in the context of an overall VCell design. Currently, VCell operates on segmented images provided by the user, because this standard data format is familiar to cell biologists and can be obtained by accessible image-processing tools. Our method, therefore, was developed for pixilated surfaces obtained from segmented images. It does not require a smooth watertight surface. Rather, the centers of the staircase facets are used directly as computational nodes, allowing for the fully conservative coupling of surface diffusion to processes in the embedding space. Because the nodes do not lie on the true surface, the approximated normals include oscillating sampling errors ("quantization" noise). While this noise leads to a diverging truncation error, the solution converges with an order between 1 and 2, due in part to mass conservation built in the algorithm.

A relatively low order of convergence of the method can be improved in the future by adapting our solver to the cases in which smoother surfaces are available as an input, either because a smoothing procedure has been applied, or because the image is highly resolved. In those cases, a more accurate approximation of normals could be achieved. Also, the computational nodes might be located closer to the true surface than in the case of a staircase approximation. The algorithm presented in this paper can still be applied by replacing the current method of computing normals with a more accurate approximation. Arc lengths would be calculated with higher accuracy, and the overall accuracy of the algorithm would improve. It is important to bear in mind, though, that biological data are at best within 5–10% error, and the present method produces results

in this error range on a relatively coarse mesh. Thus, the benefit of gaining accuracy should be weighed against development effort and computational cost.

In part II of the paper, the method is applied to simulate fluorescence loss in photobleaching in the geometry of a real cell. This modeling study validates assumptions that underlie a simple and fast analysis of FLIP data proposed in [17] for inferring parameters of the protein–membrane interaction.

Acknowledgements

We thank Leslie Loew for continuing support and stimulating discussions throughout the project, and Mark Terasaki and Ann Cowan for helpful comments on modeling FLIP. Frank Morgan developed tools for visualizing and exporting simulation results and helped reconstruct cell geometry from experimental images. Ion Moraru helped with exporting data at early stages of the work. The application part would not be possible without help and advice from Kostas Moissoglu and Martin Schwartz. The work is supported through Grants P41-RR13186 and U54-GM64346 from National Institutes of Health.

Appendix. Computation of normal vectors

Because the normal vector $\mathbf{N}$ at a given node $\mathbf{r}_i$ is a cross-product of two non-collinear vectors in the tangential plane at this node, the problem reduces to approximating the tangential vectors. In our algorithm, we approximate the tangents to the contours obtained by dissecting the surface at $\mathbf{r}_i$ in the two Cartesian directions, as shown in Fig. 1 of the main text where the contours are the "staircases" γ_1 and γ_2.

Consider one of them (Fig. A0). The set of nodes $\{\mathbf{R}_i\}$ on this contour is always a subset of $\{\mathbf{r}_i\}$. The tangent vector $\boldsymbol{\tau}_i$ at a given node $\mathbf{R}_i$ can be approximated using its local neighbors, $\mathbf{R}_{i+k}$ and $\mathbf{R}_{i-k}$, that are k steps apart from $\mathbf{R}_i$,

$$\boldsymbol{\tau}_i = \frac{\mathbf{R}_{i+k} - \mathbf{R}_{i-k}}{|\mathbf{R}_{i+k} - \mathbf{R}_{i-k}|} \tag{A.1}$$

The optimal choice of k in (A.1) minimizes the total error in $\boldsymbol{\tau}_i$ that includes the truncation error due to the finite difference approximation, and the sampling error. We use $p = \int |\mathrm{d}x| + |\mathrm{d}y|$ to parameterize the original smooth contour $\mathbf{R}_0(p)$. Let $\mathbf{R}_0(p_i)$ be the point on this contour closest to $\mathbf{R}_i$. With the notation: $\Delta p = kh$, $\boldsymbol{\xi}_+ = \mathbf{R}_{i+k} - \mathbf{R}_0(p_i + \Delta p)$, and $\boldsymbol{\xi}_- = \mathbf{R}_{i-k} - \mathbf{R}_0(p_i - \Delta p)$,

$$\mathbf{R}_{i+k} - \mathbf{R}_{i-k} = \mathbf{R}_0(p_i + \Delta p) - \mathbf{R}_0(p_i - \Delta p) + \boldsymbol{\xi}_+ - \boldsymbol{\xi}_- \approx 2\mathbf{R}_0'(p_i)\Delta p + \frac{1}{3}\mathbf{R}_0'''(p_i)(\Delta p^3) + \boldsymbol{\xi}_+ - \boldsymbol{\xi}_- \tag{A.2}$$

Because $|\boldsymbol{\xi}_+|, |\boldsymbol{\xi}_-| = \mathrm{O}(h)$ and $\boldsymbol{\tau}_i^0 = \mathbf{R}_0'(p_i)/|\mathbf{R}_0'(p_i)|$, the total error $|\boldsymbol{\tau}_i - \boldsymbol{\tau}_i^0| = \mathrm{O}(\Delta p^2) + \mathrm{O}(h/\Delta p)$. The minimum of the error is then achieved when $\Delta p = \mathrm{O}(h^{1/3})$ and $k \equiv \Delta p/h = \mathrm{O}(h^{-2/3})$. More precisely, we choose k

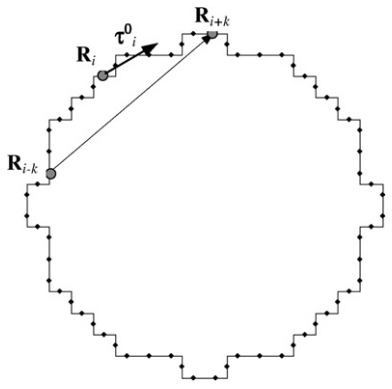

Fig. A0. Contour γ_1 from Fig. 2 of the main text.

and Δp as $k = (\rho/h)^{2/3}$ and $\Delta p = \rho^{2/3}h^{1/3}$, where ρ is the local radius of curvature on the original smooth curve. With the optimal choice of k, the error converges to zero as $O(h^{2/3})$.

In general, ρ and the optimal k vary from node to node. We estimate $\rho(\mathbf{R}_i) \equiv \rho_i$ by the radius of a circle circumscribed in the triangle $[\mathbf{R}_{i-k}, \mathbf{R}_i, \mathbf{R}_{i+k}]$ with $k = h^{-2/3}$,

$$\rho_i = \frac{|\mathbf{R}_{i-k} - \mathbf{R}_i||\mathbf{R}_i - \mathbf{R}_{i+k}||\mathbf{R}_{i+k} - \mathbf{R}_{i-k}|}{2\|\mathbf{R}_{i-k} \times \mathbf{R}_i + \mathbf{R}_i \times \mathbf{R}_{i+k} + \mathbf{R}_{i+k} \times \mathbf{R}_{i-k}\|}$$

provided it does not exceed half the dimension of the contour, $d = \max_{i,j}|\mathbf{R}_i - \mathbf{R}_j|$, otherwise $\rho_i = d/2$. The accuracy of the normal vector $\mathbf{N}$ is determined by the accuracy of $\boldsymbol{\tau}$ and therefore has the same order, $O(h^{2/3})$.

In the case of open surfaces, the tangents at the boundary points are approximated with accuracy $|\boldsymbol{\tau}_i - \boldsymbol{\tau}_i^0| = O(\Delta p) + O(h/\Delta p)$ because the scheme is not centered. This yields an optimal $k = (\rho/h)^{1/2}$. Since in our tests, both $k = (\rho/h)^{2/3}$ and $k = (\rho/h)^{1/2}$ produced results of comparable accuracy for closed surfaces, the algorithm implemented in the VCell uses $k = (\rho/h)^{1/2}$ for all nodes. All the test results in Section 2.5 were obtained with this algorithm.

References

[1] P. Schwartz, D. Adalsteinsson, P. Colella, A.P. Arkin, M. Onsum, Numerical computation of diffusion on a surface, Proc. Natl. Acad. Sci. USA 102 (2005) 11151–11156.

[2] I.F. Sbalzarini, A. Hayer, A. Helenius, P. Koumoutsakos, Simulations of (an)isotropic diffusion on curved biological surface, Biophys. J. 90 (2006) 878–885.

[3] B. Alberts, A. Johnson, J. Lewis, M. Raff, K. Roberts, P. Walter, Molecular Biology of the Cell, third ed., Garland Publ., New York, 1994.

[4] S. Rosenberg, The Laplacian on a Riemannian Manifold, University Press, Cambridge, 1997.

[5] G.L. Xu, Convergence of discrete Laplace–Beltrami operators over surfaces, Comput. Math. Appl. 48 (2004) 347–360.

[6] D. Adalsteinsson, J.A. Sethian, Transport and diffusion of material quantities on propagating interfaces via level set methods, J. Comput. Phys. 185 (2003) 271–288.

[7] M. Bertalmio, L.-T. Cheng, S. Osher, G. Sapiro, Variational problems and partial differential equations on implicit surfaces, J. Comput. Phys. 174 (2001) 759–780.

[8] I.F. Sbalzarini, A. Mezzacasa, A. Helenius, P. Koumoutsakos, Effects of Organelle Shape on Fluorescence Recovery after Photobleaching, Biophys. J. 89 (2005) 1482–1492.

[9] J.B. Greer, An Improvement of a Recent Eulerian Method for Solving PDEs on General Geometries, J. Sci. Comput. 29 (2006) 321–351.

[10] A. Ratz, A. Voigt, PDE's on surfaces – a diffuse interface approach, Commun. Math. Sci. 4 (2006) 575–590.

[11] M. Pauly, L.P. Kobbelt, M. Gross, Point-based multiscale surface representation, ACM Trans. Graphics 25 (2006) 177–193.

[12] M. Christensen, How to simulate anisotropic diffusion processes on curved surfaces, J. Comput. Phys. 201 (2004) 421–438.

[13] R. Holyst, D. Plewczynski, A. Aksimentiev, K. Burdzy, Diffusion on curved, periodic surfaces, Phys. Rev. E 60 (1999) 302–307.

[14] B.M. Slepchenko, J.C. Schaff, I. Macara, L.M. Loew, Quantitative cell biology with the Virtual Cell, Trends Cell Biol. 13 (2003) 570–576.

[15] B.M. Slepchenko, J.C. Schaff, Y.S. Choi, Numerical approach to fast reactions in reaction–diffusion systems: application to buffered calcium waves in bistable models, J. Comput. Phys. 162 (2000) 186–218.

[16] J.C. Schaff, B.M. Slepchenko, Y.-S. Choi, J. Wagner, D. Resasco, L.M. Loew, Analysis of nonlinear dynamics on arbitrary geometries with the Virtual Cell, Chaos 11 (2001) 115–131.

[17] K. Moissoglu, B.M. Slepchenko, N. Meller, A.F. Horwitz, M.A. Schwartz, In vivo dynamics of Rac–membrane interactions, Mol. Biol. Cell 17 (2006) 2770–2779.

[18] J.H. Ferziger, M. Peric, Computational Methods for Fluid Dynamics, third ed., Springer, 2002.

[19] Q. Du, L. Ju, A finite volume method on general surfaces and its error estimates, Numerische Mathematik, submitted for publication.

[20] G.Leibon, D. Letscher, Delaunay triangulations and Voronoi diagrams for riemannian manifolds, in: Proceedings of the 16th Annual Symposium on Computational Geometry (Hong Kong, 2000), pp. 341–349.

[21] N. Sukumar, Voronoi cell finite difference method for the diffusion operator on arbitrary unstructured grids, Int. J. Numer. Meth. Eng. 57 (2003) 1–34.

[22] I.D. Mishev, Finite volume methods on Voronoi meshes, Numer. Meth. Partial Diff. Equat. 14 (1998) 193–212.

[23] L. Van Aelst, C. D'Souza-Schorey, Rho GTPases and signaling networks, Genes Dev. 11 (1997) 2295–2322.

[24] B. Olofsson, Rho guanine dissociation inhibitors: pivotal molecules in cellular signaling, Cell Signal 11 (1999) 545–554.

[25] G. Taubin, T. Zhang, G. Golub, Optimal surface smoothing as filter design, in: Proceedings of the 4th European Conference on Computer Vision, vol. 1, (1996) pp. 283–292 .

[26] M. Arrio-Dupont, G. Foucault, M. Vacher, P.E. Devaux, S. Cribier, Translational diffusion of globular proteins in the cytoplasm of cultured muscle cells, Biophys. J. 78 (2000) 901–907.
[27] J. Wagner, J. Keizer, Effect of rapid buffers on Ca^{2+} diffusion and oscillations, Biophys. J. 67 (1994) 447–456.
[28] I.L. Novak, B.M. Slepchenko, A. Mogilner, L.M. Loew, Cooperativity between cell contractility and adhesion, Phys. Rev. Lett. 93 (2004) 268109.